

Enhanced conduction and charge-selectivity by N-doped graphene flakes in the active layer of bulk-heterojunction organic solar cells†

Cite this: *Energy Environ. Sci.*, 2013, **6**, 3000

Gwang Hoon Jun,^a Sung Hwan Jin,^a Bin Lee,^a Bo Hyun Kim,^a Weon-Sik Chae,^b Soon Hyung Hong^{*a} and Seokwoo Jeon^{*a}

Polymeric organic photovoltaic (OPV) cells are promising candidates for low-cost, high-performance energy sources due to their low material and processing costs, flexibility, and ease of manufacturing by solution processes. However, low power-conversion efficiency (PCE) has impeded the development of OPV cells. The low PCE in OPV solar cells has been attributed to low carrier mobility, which is related to the transport length of the charge carriers within active layers. Graphene can be an ideal material for assisting the charge transport in the active layer of OPV cells due to its excellent charge carrier mobility, thermal and chemical stability, and compatibility with the solution process. In this work, we demonstrated for the first time an improvement of the PCE (up to 40%) in OPV bulk-heterojunction (BHJ) cells by incorporating charge-selective graphene flakes into the BHJ active layer. The charge selectivity of graphene flakes was achieved by nitrogen doping (N-doped graphene). The N-doped graphene, when mixed in the active layer (N-doped graphene/polymer:fullerene composites), provided transport pathways exclusively to specific charge carriers through the modulation of band-gap structures. We discuss further the enhancement of the PCE in OPV cells with respect to charge-carrier mobility.

Received 20th March 2013

Accepted 2nd July 2013

DOI: 10.1039/c3ee40963e

www.rsc.org/ees

Broader context

Organic solar cells have received a lot of attention due to their low production costs, easy scalability to large-areas and applicability on flexible substrates. One of the main challenges to widespread application in practical devices is their low power conversion efficiency (PCE). This is largely because of the low charge-carrier mobilities and poor charge transfer characteristics in organic materials, resulting in short carrier lifetimes and reduced charge collection efficiencies. In this work, we demonstrate that the use of nitrogen-doped graphene improves the power conversion efficiency of a bulk-heterojunction solar cell system. The nitrogen-doped graphene provides transport pathways to specific charge carriers through the modulation of band structures when mixed into the active layer. We believe that the added functionality of charge selectivity in conductive graphene flakes gives a new design parameter for increasing the PCE of bulk-heterojunction solar cells.

1 Introduction

Polymeric organic photovoltaic (OPV) cells are promising candidates for low-cost, high-performance energy sources due to their low material and processing costs, flexibility, and ease of manufacturing by solution processes.^{1–3} However, the low power-conversion efficiency (PCE) of OPV cells due to the extremely short length of exciton diffusion (~ 10 nm) in the organic active layers has impeded their progress toward becoming a leading alternative energy source.⁴ Structural advances in solution-

processed bulk-heterojunction (BHJ) solar cells have provided a means to maximize the exciton dissociation by matching the typical exciton diffusion length (~ 10 nm).^{4,5} In BHJ solar cells, nanoscale phase separation of donors and acceptors within the exciton diffusion length increases the opportunity for excitons to dissociate into charge carriers, resulting in better PCE.^{5,6} To date, numerous studies on the PCE of OPV cells have identified the origins of low PCE in OPV-BHJ solar cells: the misalignment of energy levels between the donor and acceptor, insufficient light absorption in the active layer, a short exciton diffusion length, and low carrier mobility in the phase-separated layers of the BHJ.^{7,8} Among these, low carrier mobility is the predominant factor underlying low PCE. Due to the low electron and hole mobilities of the polymer materials ($< 10^{-4}$ cm² V⁻¹ s⁻¹), the separated charge carriers are eliminated by recombination or charge trapping before arriving at the electrodes.^{6,9} During the past decade, carbon-based nanomaterials such as carbon

^aDepartment of Materials Science and Engineering, Korea Advanced Institute of Science and Technology, Daejeon, 305-701, Republic of Korea. E-mail: jeon39@kaist.ac.kr; Fax: +82 42 350 3310; Tel: +82 42 350 3342

^bGangneung Center, Korea Basic Science Institute, Gangneung 210-702, Republic of Korea

† Electronic supplementary information (ESI) available: See DOI: 10.1039/c3ee40963e

nanotubes (CNTs) have been adopted to provide conductive pathways in the active layer due to their extremely high carrier mobility.^{10–14} Berson *et al.* incorporated single-walled nanotubes (SWNTs) or multi-walled nanotubes (MWNTs) into a BHJ solar cell to facilitate exciton dissociation and charge extraction and demonstrated a PCE of ~2%.¹¹ Chaudhary *et al.* reported on a layered device composed of a carbon nanotube (CNT) network embedded in a poly(3-hexylthiophene) (P3HT)/[6,6]-phenyl-C61-butyric acid methyl ester (PCBM) active layer.¹² However, this yielded low performance and a reduced short-circuit current (J_{SC}) because the nonhomogeneous dispersion of the CNT network disrupted the optimized morphology of the phase-separated active layer. As noted, one of the major challenges in incorporating CNTs into OPV cells is the agglomeration of CNTs resulting from their low dispersibility in the active layer, which significantly decreases device performance. Previously, we reported that the incorporation of highly dispersed SWNTs by covalent functionalization significantly improved PCE, which was attributed to the efficient charge carrier pathways in the active layer provided by SWNTs.¹³

Graphene, a two-dimensional carbon material, has received considerable attention recently due to its excellent charge-carrier mobility,^{15,16} thermal and chemical stability,^{17,18} and compatibility with organic materials and solution processes.^{19–21} Moreover, graphene can promote more efficient charge-carrier transport compared with CNTs because the two-dimensional (2-D) plane of graphene has a much larger specific surface area than that of CNTs. Thus, numerous interfaces can be created when graphene is added to a polymer matrix. From this perspective, graphene may be an ideal material for facilitating charge transport in the active layer of OPVs.^{22–24} However, work in this area has not, to the best of the authors' knowledge, been described previously. This may be due, in part, to the amphoteric conduction of graphene; without proper doping of graphene, insufficient charge separation and undesired electron-hole recombination can deteriorate cell performance. In a previous study of a CNT-OPV hybrid active layer, embedded CNTs without good charge selectivity degraded the performance of OPV devices through charge-carrier recombination on the metallic CNTs in the active layer.²⁵ Accordingly, the key challenge to using graphene in OPV cells as a charge-transport material is enhancing the charge selectivity of graphene.

In this work, we demonstrated an improvement of the PCE in OPV-BHJ cells by incorporating charge-selective graphene flakes into the BHJ active layer. The charge selectivity of the graphene flakes was achieved by nitrogen doping (N-doped graphene). N-doped graphene provides transport pathways exclusively to specific charge carriers (electrons) through the modulation of band-gap structures when mixed in the active layer (N-doped graphene/polymer:fullerene composites). The doping ratio and chemical properties of graphene are examined by Raman spectroscopy and X-ray photoelectron spectroscopy (XPS). The PCE of the OPV cell with N-doped graphene was enhanced by 40% compared with an organic solar cell without graphene. Also, the PCE with respect to the ratio of N-doped graphene in the active layer was compared with that of reduced graphene oxide (RGO) without doping the incorporated OPV cells.

2 Experimental

2.1 Fabrication process of graphene oxide

Graphene oxide (GO) was fabricated using the modified Hummers method. Graphite (SP-1, Bay carbon) and H_2SO_4 (95%, Junsei extra pure grade) were mixed in an ice bath. $KMnO_4$ (Aldrich), an oxidizing agent, was added slowly to the graphite solution. After thorough mixing, deionized (DI) water was added to the solution as an oxygen source. HCl solution (10%, mixed with DI water) was used to rinse and remove the residue.

2.2 Reduction of graphene oxide by H_2 annealing

H_2 and NH_3 annealing processes of GO were carried out in a tube furnace. We used ultra-high-purity (99.999%) H_2 and NH_3 . GO samples were placed in the center of the tube furnace. After flowing H_2 for ~5 min, the samples were placed in a 300 °C furnace for 15 min and then directly heated to the reaction temperature. The reaction temperature was maintained for 10 min. The samples were taken out after the furnace had cooled to <50 °C.

2.3 Nitrogen-doping process of graphene oxide by NH_3 annealing

The NH_3 annealing process proceeded as follows. GO samples were placed in the center of a tube furnace. After flowing NH_3 for ~5 min, the samples were placed in a 300 °C furnace for 15 min and then heated to the reaction temperature. The reaction temperature was maintained for 10 min inside the furnace before cooling. The samples were taken out of the tube reactor after the furnace temperature cooled to <50 °C.

2.4 Fabrication of graphene/P3HT:PCBM nanocomposites

The reduced graphene oxide (RGO) and N-doped RGO (N-RGO) were diluted to 1 mg for every 10 mL in chlorobenzene by 1 h sonication. P3HT (Rieke Metals) and [6,6]-phenyl-C61-butyric acid methyl ester (PCBM) (Sigma Aldrich) were dissolved and stirred in 1 mL of chlorobenzene for 12 h. Varying amounts of P3HT (0, 0.2, 0.5, and 1.0 wt%) were added to RGO and N-RGO.

2.5 Fabrication of OPVC using graphene/P3HT:PCBM nanocomposites

Indium tin oxide (ITO)-coated glass was cleaned with 2-propanol and a mixture of NH_3 and H_2O_2 . O_2 plasma treatment was used to enhance the wetting between ITO and poly(3,4-ethylenedioxythiophene):poly(styrenesulfonate) (PEDOT:PSS) purchased from Sigma Aldrich. PEDOT:PSS was spin-coated onto ITO at 1000 rpm for 1 min and then baked at 120 °C for 10 min. P3HT and PCBM were dissolved and stirred in 1 mL of chlorobenzene for 12 h. RGO and N-RGO were mixed with a P3HT:PCBM (1.0 : 0.8) blend, which was made by mixing the two solutions for 12 h. The blend of RGO and N-RGO, P3HT, and PCBM was spin-coated onto the PEDOT:PSS at 300 rpm for 1 min in a glove box filled with N_2 gas. An Al electrode was thermally evaporated onto the device in a vacuum (pressure: 10^{-7} Torr). Finally, the device was annealed at 150 °C for 5 min.

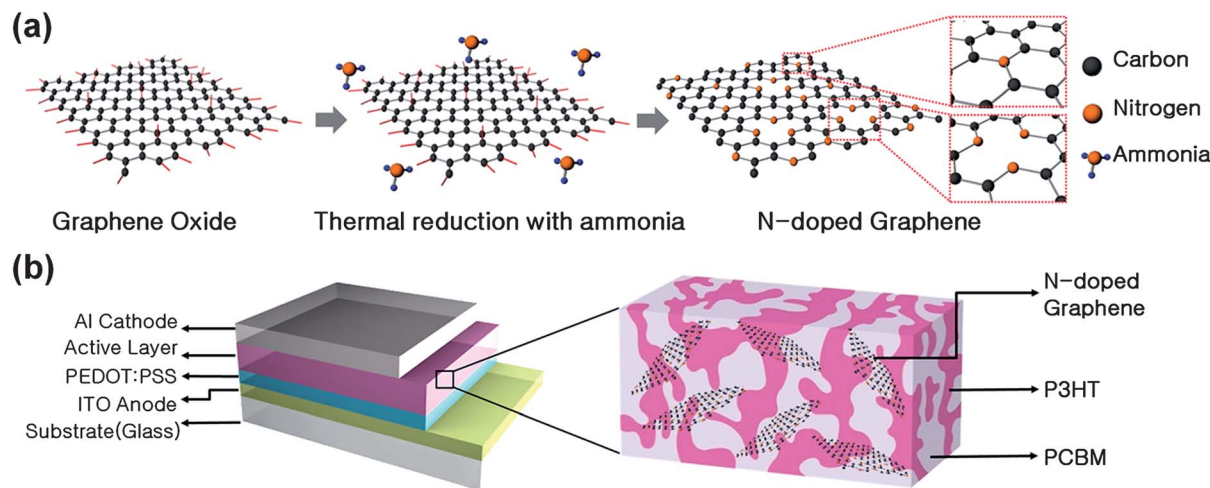


Fig. 1 Schematic of the nitrogen doping process of RGO (a) and the BHJ solar cell using the N-doped graphene/P3HT:PCBM active layer fabricated in this work (b).

2.6 Characterization

The surface functional groups of the samples were characterized by XPS (Sigma Probe). The work function of the reduced graphene was obtained by ultraviolet photoelectron spectroscopy (UPS, Sigma Probe). Raman spectroscopy was performed using a high-resolution dispersive Raman microscope (LabRAM HR UV/Vis/NIR, excitation: 514 nm). Fluorescence lifetime image microscopy was performed using an inverted-type scanning confocal microscope (MicroTime-200, Picoquant, Germany). A single-mode pulsed diode laser (wavelength: 470 nm; instrumental response function: ~ 96 ps full-width at half-maximum; repetition rate: 40 MHz) was used as the excitation source. A dichroic mirror (490 DCXR, AHF), a long-pass filter (HQ500lp, AHF), a 50 μm pinhole, and a single-photon avalanche diode were used to collect the emissions ($\lambda > 500$ nm). The photovoltaic properties of the OPV cell were characterized under 1-sun output power, using a xenon lamp with an air mass global filter (AM 1.5). A silicon reference solar cell certified by the National Renewable Energy Laboratory (NREL) was used to calibrate the light and confirm the measurement conditions. Current-voltage (I - V) measurements were performed using an electrochemical analyzer (CompactStat, Ivium Technologies). The entire test is repeated for the four devices for each set of fabrication conditions.

3 Results and discussion

Fig. 1(a) shows a schematic illustration of the N-doping process of graphene. The process is a simple, well-studied, doping method used to control the local electronic structures and energy band gap of graphitic carbon.^{26–28} For N doping, GO was reduced *via* thermal treatment with N_2/NH_3 gas. During the thermal reduction process of GO under ammonia conditions, nitrogen atoms formed pyridine-like (N-P) and graphite-like (N-Q) N configurations through substitutions of carbon atoms (inset of Fig. 1(a)).²⁷ It is known that N-Q improves the electroconductivity of graphene films by providing delocalized

electrons, whereas N-P, having a localized lone pair of electrons, creates vacancy-type defects that interrupt the graphitic sp^2 structure.^{29,30} N-RGO was dispersed in organic solvents and mixed with P3HT and PCBM in a solution state. Finally, the N-RGO/P3HT:PCBM solution was deposited as an active layer by a spin-coating process. Fig. 1(b) shows a schematic illustration of a P3HT:PCBM bulk-heterojunction cell with N-doped graphene incorporated into the active layer.

The doping state of graphene was examined by Raman spectroscopy and XPS. Fig. 2 shows the Raman spectra of RGO and N-RGO. Two characteristic graphene peaks, the G and D bands shown near 1590 cm^{-1} and 1350 cm^{-1} , respectively, were observed in the Raman spectra of both RGO and N-RGO. The peak of the G band in N-RGO was slightly downshifted with respect to that in RGO, whereas the peak position of the D band in RGO and N-RGO remained unchanged. It is known that the G-band shift is affected by doping,^{31–33} the type of substrate,³⁴ defects,³⁵ strains,^{36–38} and layer number.^{39–41} Our results are in good agreement with those observed from N-doped CNTs, in which N doping induced a downshift of the G band in the Raman spectrum.⁴² Wei *et al.* previously reported that the electron-donating ability determines the amount of charge

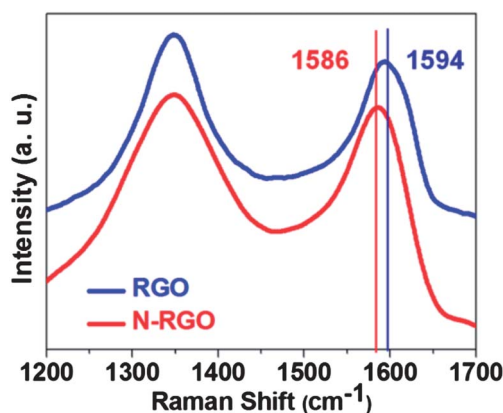


Fig. 2 Raman spectra of RGO (blue) and N-RGO (red).

transfer and modifies the position of the G band.³⁰ Accordingly, the thermal reduction process of GO with NH_3 in this experiment facilitates doping of RGO by nitrogen, providing delocalized electrons to the graphene surface. Additionally, the relatively high intensity of the G band (compared with the D band) in N-RGO suggests that N-RGO is in a more reduced state relative to RGO.

The peaks in the XPS spectra verified N doping of RGO. Fig. 3(a) shows a comparison of the XPS spectra between graphite, GO, RGO, and N-RGO. In GO and RGO, carbon and oxygen peaks were observed; however there was no nitrogen peak. Meanwhile, in the N-RGO spectrum, an $\sim 5\%$ oxygen peak and an $\sim 8\%$ nitrogen peak were observed together with other carbon content (see ESI, Table S1†). Fig. 3(b) and (c) show the C1s spectra of RGO and N-RGO, respectively. The C1s peak was deconvoluted, based on atomic bonding. The peak at 284.5 eV was related to the pure sp^2 carbon-carbon (C-C) bond, and the

peak at 287–288 eV was ascribed to oxygenated carbon atoms. The results obtained from the C1s spectra suggest that there were oxygen-containing groups on the graphene surface after the reduction process. This is in line with previous results indicating that at least 3–5 atomic% oxygen remained on graphene, because the reduction process of GO was incomplete.¹⁹ In N-RGO, another peak at 285.8 eV indicating a C-N bond provides evidence of N doping by thermal reduction under ammonia conditions. Because N-Q is more desirable than N-P for its electroconductivity, as mentioned before, it is worth noting that the proportion of N-Q achieved from the narrow scanning of nitrogen increased two-fold relative to that of N-P under optimized thermal-reduction conditions (see ESI, Fig. S1 and Table S2†). The optimized reduction process guarantees the charge selectivity of the N-doped graphene flakes.

Incorporation of N-doped graphene into the active layer in OPV-BHJ cells is hypothesized to improve the PCE due to its

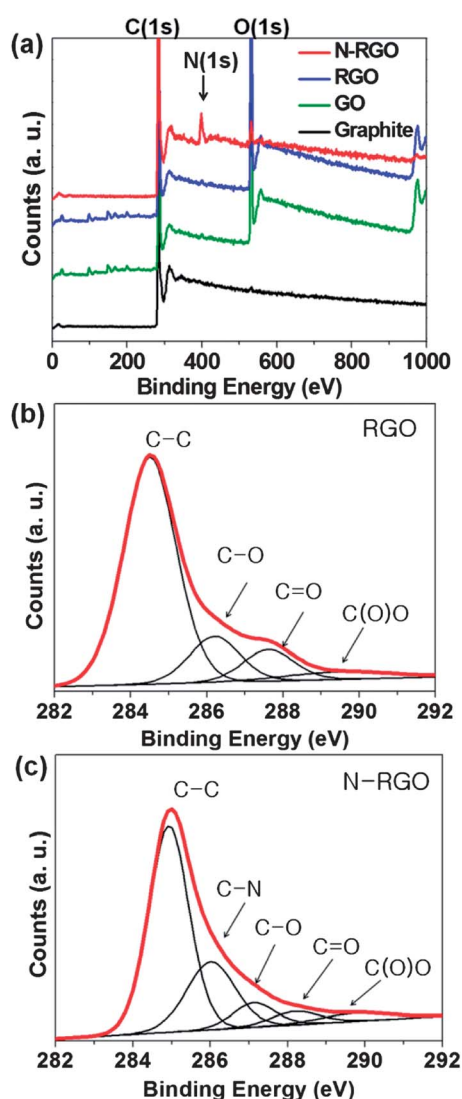


Fig. 3 (a) XPS spectra of graphite (black), GO (green), RGO (blue) and N-RGO (red). XPS spectra of C (1s) peaks. High resolution C (1s) spectra of RGO (b) and N-RGO (c).

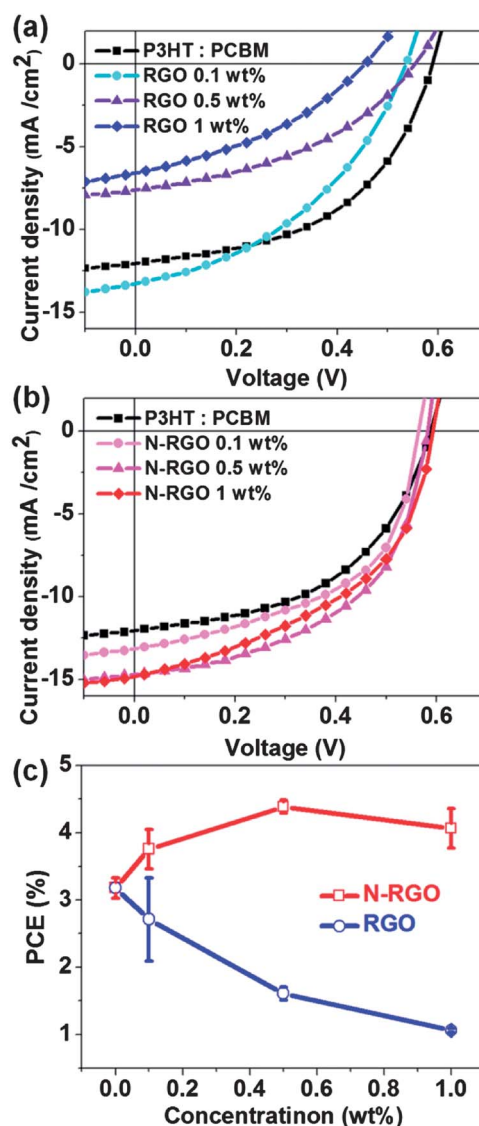


Fig. 4 Current density–voltage (J – V) characteristics of devices as a function of RGO (a) and N-RGO (b) concentration. The power conversion efficiency as a function of RGO (blue) and N-RGO (red) concentration (c).

charge-carrier pathways, which support electron transfer between PCBM molecules. To verify this, the electrical properties of the fabricated devices shown in Fig. 1(b) were measured. Fig. 4(a) and (b) show the I - V characteristics of OPV-BHJ cells under AM 1.5-simulated solar radiation, according to the ratio of RGO and N-RGO in the active layer, respectively. Whereas the PCE of RGO/PCBM composites decreased significantly with increased wt% RGO, the PCE of N-RGO/PCBM composites improved from 3.2 to 4.5% as N-RGO increased from 0.1 to 0.5 wt%. This PCE value was also higher than that of the reference solar cell using P3HT:PCBM without graphene. From the I - V characteristic curves, the PCE was extracted and plotted as a function of graphene concentration (Fig. 4(c)). The increase in the PCE is in accordance with the increase in the short-circuit current J_{SC} (from 10.5 to 14.8 mA cm^{-2}). In contrast, the PCE obtained for the RGO/PCBM composites decreased due to a reduced short-circuit current. This suggests that N-RGO acted as a charge-carrier pathway, supporting electron transfer between PCBM molecules, whereas the undoped RGO offered undesirable pathways for electron-hole recombination sites. The detailed device parameters of N-RGO/PCBM composites, including the PCE, open-circuit voltage (V_{OC}), short-circuit current (J_{SC}), and fill factor (FF), are presented in Table S3.†

The highest PCE of the OPV-BHJ cells with N-RGO/PCBM can be explained based on the charge selectivity of N-RGO in the active matrix; effective charge pathways were provided by both N-RGO and RGO. The underlying mechanism of the exclusive charge pathways through N-RGO is the modulation of the work function in the energy band structure (Fig. 5). To investigate the effect of charge selectivity by the incorporated N-RGO, we measured the work function of RGO and N-RGO using UPS (see Fig. S2†). From the UPS spectra, the work function can be estimated as the energy level difference between the inelastic cutoff and the Fermi edge, as described by the following equation:

$$\Phi = E_v - |E_{\text{cutoff}} - E_f| \quad (1)$$

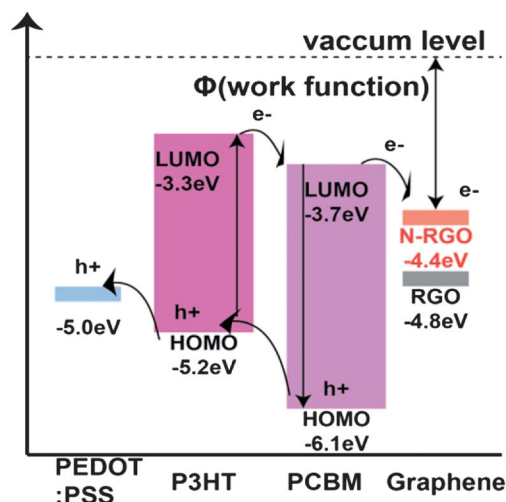


Fig. 5 Energy-level diagram of a RGO and N-RGO/PCBM OPV showing the charge generation and transfer between the two organic components to the electrodes.

where Φ is the work function, E_v is the ultraviolet energy, E_{cutoff} is the inelastic cutoff energy, and E_f is the Fermi edge. The calculated work function of undoped RGO is 4.8 eV, and that of N-RGO is 4.4 eV. Fig. 5 shows the overall energy-level diagram of an N-RGO/PCBM OPV cell, as well as the charge generation and transfer between the two organic components and the electrodes. The higher work function of N-RGO (by ~ 0.4 eV) suggests that modification of the energy level by N doping of RGO leads to more effective electron transfer pathways compared with the case of untreated RGO.

To investigate the effect of the increase in charge-carrier mobility caused by the incorporated N-RGO, we characterized mobility using the Mott-Gurney law,^{44,45} as described by

$$J = \frac{9}{8} \epsilon_r \epsilon_0 \mu \frac{V^2}{L^3} \quad (2)$$

where ϵ_r is the relative dielectric constant, ϵ_0 is the permittivity of free-space, μ is the charge-carrier mobility, V is the applied voltage, and L is the thickness of the device. The electron mobility increased by $\sim 74\%$ (3.1×10^{-7} to $5.4 \times 10^{-7} \text{ m}^2 \text{ V}^{-1} \text{ s}^{-1}$). This improvement in the mobility was attributed to the high conductivity of graphene (see ESI, Fig. S3 and Table S4†).

Fig. 6(a) and (b) show the diode factors of the solar cell as the N-RGO concentration increased. As mentioned above, the increase in the PCE mainly originated from the J_{SC} due to the enhancement of the charge carrier transport. However, over-weighting the incorporated N-RGO caused the PCE to drop significantly. The main reason for this drop of the PCE at high concentrations of N-RGO was a decrease in the FF, whereas enhancement of the J_{SC} beyond the optimum N-RGO concentration was limited. The decrease in the FF can be explained by increased leakage current. It seems that once the concentration

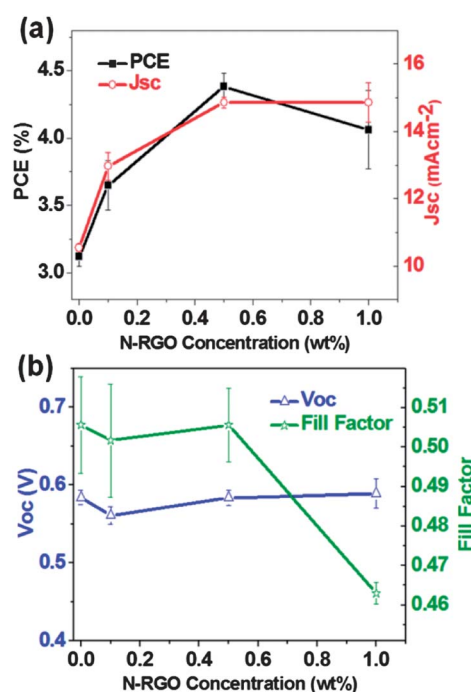


Fig. 6 Diode factors of OPV as a function of the N-RGO concentration PCE and J_{SC} (a), V_{OC} and FF (b).

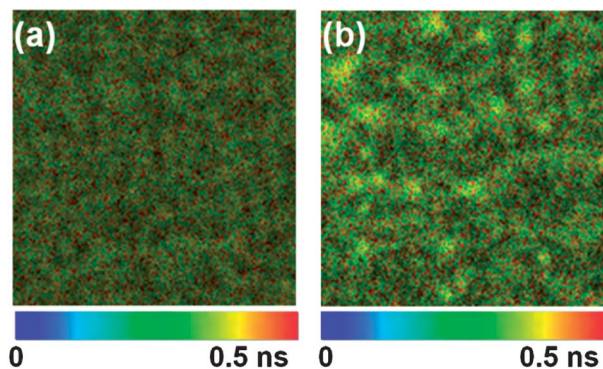


Fig. 7 2-D fluorescence-lifetime image of reference P3HT:PCBM (a) and 0.5 wt% of N-RGO (b).

of N-RGO sheets exceeds a certain value, the agglomerated sheets provide a parasitic path for the current. To confirm the tendency of increased leakage current from samples with overweight concentrations of N-RGO, we performed I - V characterization without light illumination (see ESI, Fig. S4†). Ideally, a solar cell without light illumination has no current density with an applied negative voltage due to the properties of the donor-acceptor junction. However, a device using N-RGO/P3HT:PCBM shows some leakage current, in contrast to a device using P3HT:PCBM, which showed no current with a negative voltage. This leakage current can affect the diode behavior and decrease the FF and PCE. The FF and PCE consequently decreased as a result of the increased leakage current because the agglomerated N-RGO sheets behaved as potential recombination sites.

In fact, electron transfer in polymer-fullerene solar cells is higher than that of hole transfer. The incorporation of N-RGO for better electron transfer makes the overall charge transport more imbalanced. However, even though N-RGO provided good electron transport, our results concerning the increase in J_{SC} indicated that rapid electron transfer by the charge-selective graphene sufficiently enhanced device performance because the extraction of electrons prevented recombination of electrons and holes.⁵⁰

We performed fluorescence lifetime mapping by combining a time-resolved fluorescence measurement system with a confocal laser scanning microscope to obtain the evolution of the fluorescence lifetime in the P3HT:PCBM films.⁴³ This technique enabled us to examine the distribution of the lifetimes on any given 2-D plane. Fig. 7(a) and (b) display the lifetime images ($90\ \mu\text{m} \times 90\ \mu\text{m}$) of each reference P3HT:PCBM and 0.5 wt% N-RGO/P3HT:PCBM, respectively. The brightly distinguished regions in the images are assumed to be the locations of incorporated graphene. Despite the absence of an energy gap for graphene, photoluminescence (PL) has been observed in chemically modified graphene.^{46–48} A recent study of chemically modified RGO with N doping suggested that the large increase in the intensity of the PL emission was caused by the transfer of energy from the N atoms to the sp^2 clusters in the graphene matrix.⁴⁹ Therefore, the brightly distinguished regions in the images are assumed to be the locations of incorporated

graphene. We observed that the N-RGO exhibited a highly homogeneous dispersion. These results demonstrate that the N-doping process of graphene is an effective method to disperse graphenes in a P3HT:PCBM matrix. The N-doped sites yielded local negative charges, inducing local polarity on the graphene surface. This could cause electrostatic repulsion between neighboring graphenes, enhancing the dispersibility of graphene in organic solvents and the polymer matrix.

4 Conclusions

In this work, we report an improved PCE of OPV cells using N-doped graphene flakes with better charge selectivity. The N-RGO was confirmed by XPS analysis results showing that approximately $\sim 8\%$ of the C atoms of graphene were replaced by N atoms. UPS analysis indicated that the band gap of N-RGO was modified to 4.8 eV from a value of 4.4 eV for RGO. The PCE of the OPV cell using N-RGO increased significantly from 3.2% to 4.5% without N-RGO. The fluorescence lifetime mapping experiment showed that N-doped graphene was well dispersed in the polymer matrix. Consequently, we demonstrated that the use of N-doped graphene improved the PCE of a BHJ solar cell system through higher carrier mobility of graphene with charge selectivity. We believe that the added functionality of charge selectivity in conductive graphene flakes gives a new design parameter to increase the PCE of BHJ solar cells by further improvement in the synthesis of graphene flakes (*i.e.*, conductivity, size, doping level, and defect control).

Acknowledgements

This research was supported by the WCU (World Class University) program through the National Research Foundation of Korea (R32-10051), Center for Advanced Soft Electronics under the Global Frontier Research Program (2011-0031630), and Basic Science Research Program through the National Research Foundation of Korea (CAFDC-2011-0001137) funded by the Ministry of Science, ICT & Future Planning, Science and Technology and KAIST Institute for the NanoCentury in Korea.

References

- 1 N. S. Lewis, *Science*, 2007, **315**, 798–801.
- 2 G. Yu, J. Gao, J. C. Hummelen, F. Wudl and A. J. Heeger, *Science*, 1995, **270**, 1789–1791.
- 3 G. Dennler, M. C. Scharber and C. J. Brabec, *Adv. Mater.*, 2009, **21**, 1323–1338.
- 4 B. Kannan, K. Castelino and A. Majumdar, *Nano Lett.*, 2003, **3**, 1729–1733.
- 5 W. L. Ma, C. Y. Yang, X. Gong, K. Lee and A. J. Heeger, *Adv. Funct. Mater.*, 2005, **15**, 1617–1622.
- 6 G. Li, V. Shrotriya, J. S. Huang, Y. Yao, T. Moriarty, K. Emery and Y. Yang, *Nat. Mater.*, 2005, **4**, 864–868.
- 7 K. Vandewal, K. Tvingstedt, A. Gadisa, O. Inganäs and J. V. Manca, *Nat. Mater.*, 2009, **8**, 904–909.
- 8 B. W. Ma, C. H. Woo, Y. Miyamoto and J. M. J. Frechet, *Chem. Mater.*, 2009, **21**, 1413–1417.

- 9 K. M. O'Malley, C. Z. Li, H. L. Yip and A. K. Y. Jen, *Adv. Energy Mater.*, 2012, **2**, 82–86.
- 10 S. H. Jin, G. H. Jun, S. H. Hong and S. Jeon, *Carbon*, 2012, **50**, 4483–4488.
- 11 S. Berson, R. de Bettignies, S. Bailly, S. Guillerez and B. Jousselme, *Adv. Funct. Mater.*, 2007, **17**, 3363–3370.
- 12 S. Chaudhary, H. W. Lu, A. M. Muller, C. J. Bardeen and M. Ozkan, *Nano Lett.*, 2007, **7**, 1973–1979.
- 13 G. H. Jun, S. H. Jin, S. H. Park, S. Jeon and S. H. Hong, *Carbon*, 2012, **50**, 40–46.
- 14 Q. Cao and J. A. Rogers, *Adv. Mater.*, 2009, **21**, 29–53.
- 15 J. Kwon, S. H. Lee, K. H. Park, D. H. Seo, J. Lee, B. S. Kong, K. Kang and S. Jeon, *Small*, 2011, **7**, 864–868.
- 16 S. V. Morozov, K. S. Novoselov, M. I. Katsnelson, F. Schedin, D. C. Elias, J. A. Jaszczak and A. K. Geim, *Phys. Rev. Lett.*, 2008, **100**, 016602.
- 17 X. L. Li, X. R. Wang, L. Zhang, S. W. Lee and H. J. Dai, *Science*, 2008, **319**, 1229–1232.
- 18 V. C. Tung, M. J. Allen, Y. Yang and R. B. Kaner, *Nat. Nanotechnol.*, 2009, **4**, 25–29.
- 19 S. Stankovich, D. A. Dikin, G. H. B. Dommett, K. M. Kohlhaas, E. J. Zimney, E. A. Stach, R. D. Piner, S. T. Nguyen and R. S. Ruoff, *Nature*, 2006, **442**, 282–286.
- 20 K. H. Park, B. H. Kim, S. H. Song, J. Kwon, B. S. Kong, K. Kang and S. Jeon, *Nano Lett.*, 2012, **12**, 2871–2876.
- 21 B. G. Lu, T. Li, H. T. Zhao, X. D. Li, C. T. Gao, S. X. Zhang and E. Q. Xie, *Nanoscale*, 2012, **4**, 2978–2982.
- 22 T. H. Han, Y. Lee, M. R. Choi, S. H. Woo, S. H. Bae, B. H. Hong, J. H. Ahn and T. W. Lee, *Nat. Photonics*, 2012, **6**, 105–110.
- 23 H. Park, P. R. Brown, V. Buloyic and J. Kong, *Nano Lett.*, 2012, **12**, 133–140.
- 24 Z. F. Liu, Q. Liu, Y. Huang, Y. F. Ma, S. G. Yin, X. Y. Zhang, W. Sun and Y. S. Chen, *Adv. Mater.*, 2008, **20**, 3924–3930.
- 25 H. Ago, K. Petritsch, M. S. P. Shaffer, A. H. Windle and R. H. Friend, *Adv. Mater.*, 1999, **11**, 1281–1285.
- 26 B. Biel, X. Blase, F. Triozon and S. Roche, *Phys. Rev. Lett.*, 2009, **102**, 096803.
- 27 Z. Q. Luo, S. H. Lim, Z. Q. Tian, J. Z. Shang, L. F. Lai, B. MacDonald, C. Fu, Z. X. Shen, T. Yu and J. Y. Lin, *J. Mater. Chem.*, 2011, **21**, 8038–8044.
- 28 X. L. Li, H. L. Wang, J. T. Robinson, H. Sanchez, G. Diankov and H. J. Dai, *J. Am. Chem. Soc.*, 2009, **131**, 15939–15944.
- 29 X. B. Wang, L. Q. Liu, D. B. Zhu, L. Zhang, H. Z. Ma, N. Yao and B. L. Zhang, *J. Phys. Chem. B*, 2002, **106**, 2186–2190.
- 30 D. C. Wei, Y. Q. Liu, Y. Wang, H. L. Zhang, L. P. Huang and G. Yu, *Nano Lett.*, 2009, **9**, 1752–1758.
- 31 A. Das, S. Pisana, B. Chakraborty, S. Piscanec, S. K. Saha, U. V. Waghmare, K. S. Novoselov, H. R. Krishnamurthy, A. K. Geim, A. C. Ferrari and A. K. Sood, *Nat. Nanotechnol.*, 2008, **3**, 210–215.
- 32 S. Pisana, M. Lazzeri, C. Casiraghi, K. S. Novoselov, A. K. Geim, A. C. Ferrari and F. Mauri, *Nat. Mater.*, 2007, **6**, 198–201.
- 33 B. Das, R. Voggu, C. S. Rout and C. N. R. Rao, *Chem. Commun.*, 2008, 5155–5157.
- 34 Y. Y. Zhang, J. Zhang, H. B. Son, J. Kong and Z. F. Liu, *J. Am. Chem. Soc.*, 2005, **127**, 17156–17157.
- 35 A. Das, B. Chakraborty and A. K. Sood, *Bull. Mater. Sci.*, 2008, **31**, 579–584.
- 36 X. J. Duan, H. B. Son, B. Gao, J. Zhang, T. J. Wu, G. G. Samsonidze, M. S. Dresselhaus, Z. F. Liu and J. Kong, *Nano Lett.*, 2007, **7**, 2116–2121.
- 37 M. Y. Huang, H. G. Yan, T. F. Heinz and J. Hone, *Nano Lett.*, 2010, **10**, 4074–4079.
- 38 M. Y. Huang, H. G. Yan, C. Y. Chen, D. H. Song, T. F. Heinz and J. Hone, *Proc. Natl. Acad. Sci. U. S. A.*, 2009, **106**, 7304–7308.
- 39 D. Graf, F. Molitor, K. Ensslin, C. Stampfer, A. Jungen, C. Hierold and L. Wirtz, *Nano Lett.*, 2007, **7**, 238–242.
- 40 H. Hibino, H. Kageshima, M. Kotsugi, F. Maeda, F. Z. Guo and Y. Watanabe, *Phys. Rev. B: Condens. Matter Mater. Phys.*, 2009, **79**, 125437.
- 41 R. W. Havener, H. L. Zhuang, L. Brown, R. G. Hennig and J. Park, *Nano Lett.*, 2012, **12**, 3162–3167.
- 42 G. Keskar, R. Rao, J. Luo, J. Hudson, J. Chen and A. M. Rao, *Chem. Phys. Lett.*, 2005, **412**, 269–273.
- 43 J. L. Wu, F. C. Chen, Y. S. Hsiao, F. C. Chien, P. L. Chen, C. H. Kuo, M. H. Huang and C. S. Hsu, *ACS Nano*, 2011, **5**, 959–967.
- 44 V. D. Mihailetschi, J. K. J. van Duren, P. W. M. Blom, J. C. Hummelen, R. A. J. Janssen, J. M. Kroon, M. T. Rispens, W. J. H. Verhees and M. M. Wienk, *Adv. Funct. Mater.*, 2003, **13**, 43–46.
- 45 S. Scheinert and W. Schliefske, *Synth. Met.*, 2003, **139**, 501–509.
- 46 T. Gokus, R. R. Nair, A. Bonetti, M. Bohmler, A. Lombardo, K. S. Novoselov, A. K. Geim, A. C. Ferrari and A. Hartschuh, *ACS Nano*, 2009, **3**, 3963–3968.
- 47 Z. T. Luo, P. M. Vora, E. J. Mele, A. T. C. Johnson and J. M. Kikkawa, *Appl. Phys. Lett.*, 2009, **94**, 111909.
- 48 G. Eda, Y. Y. Lin, C. Mattevi, H. Yamaguchi, H. A. Chen, I. S. Chen, C. W. Chen and M. Chhowalla, *Adv. Mater.*, 2010, **22**, 505–509.
- 49 J. W. Chiou, S. C. Ray, S. I. Peng, C. H. Chuang, B. Y. Wang, H. M. Tsai, C. W. Pao, H. J. Lin, Y. C. Shao, Y. F. Wang, S. C. Chen, W. F. Pong, Y. C. Yeh, C. W. Chen, L. C. Chen, K. H. Chen, M. H. Tsai, A. Kumar, A. Ganguly, P. Papakonstantinou, H. Yamane, N. Kosugi, T. Regier, L. Liu and T. K. Sham, *J. Phys. Chem. C*, 2012, **116**, 16251–16258.
- 50 J. M. Lee, J. S. Park, S. H. Lee, H. Kim, S. Yoo and S. O. Kim, *Adv. Mater.*, 2011, **23**, 629–633.